Dalton Transactions

ROYAL SOCIETY OF CHEMISTRY

PAPER

View Article Online
View Journal | View Issue

Cite this: *Dalton Trans.*, 2025, **54**, 8086

Photoinduced energy and electron transfer processes in a supramolecular system combining a tetrapyrenylporphyrin derivative and arene–ruthenium metalla-prisms†

Santiago Luis Pons Alles, [a] Daniele Veclani, [b] Andrea Barbieri, [b] Bruno Therrien *[a] and Barbara Ventura *[b]

Received 11th November 2024,
Accepted 8th January 2025

DOI: 10.1039/d4dt03154g

rsc.li/dalton

A supramolecular system, consisting of a tetrapyrenylporphyrinic core surrounded by arene–ruthenium prisms, has been assembled and characterized by means of electrochemical and photophysical techniques. The photophysical study shows that quantitative energy transfer from the peripheral pyrenyl units towards the central porphyrin core is operative in the tetrapyrenylporphyrinic system. Interestingly, encapsulation of the pyrenyl units into the ruthenium cages affects the photophysics of the central porphyrin component, since its emission quantum yield is reduced in the supramolecular array. Femtosecond transient absorption analysis evidenced a complex interplay of deactivation pathways, including energy and electron transfer processes from the porphyrin to the metalla-prisms, associated with different conformations of the system allowed by the flexibility of the linkers. Moreover, the non-emissive arene–ruthenium cages present a peculiar excited-state dynamics, here disentangled for the first time by means of transient absorption investigations.

Introduction

Ruthenium-based complexes have been used in many fields, such as catalysis,[1,2] solar energy conversion,[3] imaging and sensing,[4,5] as well as in medicinal chemistry.[6–9] Arene–ruthenium complexes are an important family of coordination compounds, in which the metal is stabilized in a +2 oxidation state by an aromatic ligand (arene) which occupies three of the six coordination sites, limiting the introduction of other ligands. However, these additional ligands can modify the properties of the complexes,[10] and accordingly, their biological and photophysical properties. The three remaining sites are positioned at 90° from each other, allowing for the formation of shape-controlled supramolecular assemblies.[11] Accordingly, depending on the ligand used, different structures can be obtained through self-assembly of the different building blocks, including 3D structures such as rectangular, prismatic or cubic assemblies.[12–14] Some of these 3D architectures possess an internal hydrophobic cavity of tuneable size that can accomodate planar aromatic molecules,[15–17] which are primarily interacting with the host by π–π interactions.

The combination of coordination complexes with fluorophores has raised interest in recent years.[18] Indeed, self-assembled supramolecular structures offer an efficient strategy for the construction of energy transfer systems,[19–23] including systems based on fluorescence resonance energy transfer (FRET). FRET is a nonradiative energy transfer process taking place between two fluorophores, in which the excitation energy can be transferred from an excited donor to a nearby ground-state acceptor, through nonradiative dipole–dipole coupling.[18,24,25] This process is highly dependent on the donor–acceptor distance, which makes FRET interesting for applications in many fields such as light harvesting,[26] fluorescence sensing/imaging,[27,28] or determination of intermolecular interactions in biological systems.[29,30]

Multi-step FRET systems have gained interest as they possess advantages over one-step FRET systems, such as the possibility of monitoring longer range (>10 nm) interactions and higher efficiency of long-range energy transfer.[18,25] Arene–ruthenium metalla-assemblies represent an interesting scaffold for the construction of multi-step FRET systems, as they offer many options in terms of number, location and nature of fluorophores. Host–guest interactions are particularly relevant in this context, as organic fluorophores can be

[a]*Institute of Chemistry, University of Neuchâtel, Avenue de Bellevaux 51, CH-2000 Neuchatel, Switzerland. E-mail: Bruno.Therrien@unine.ch*
[b]*Institute for Organic Synthesis and Photoreactivity (ISOF) – National Research Council (CNR), Via P. Gobetti 101, 40129 Bologna, Italy. E-mail: barbara.ventura@isof.cnr.it*

†Electronic supplementary information (ESI) available: 1D and 2D NMR spectra, electrochemical, photophysical and theoretical data. See DOI: https://doi.org/10.1039/d4dt03154g

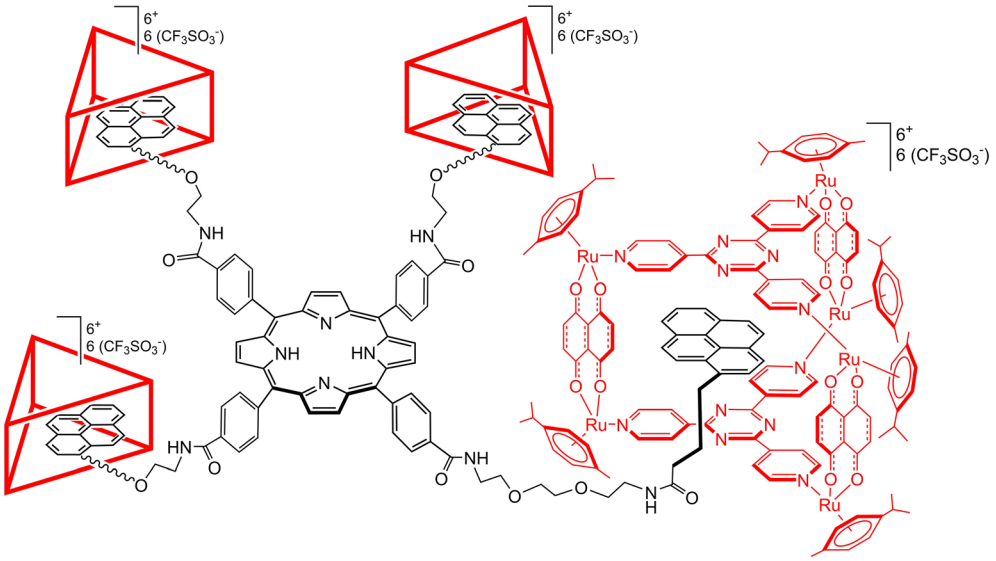

Fig. 1 Schematic representation of the **P-Pyr$_4$@(Rucage)$_4$** hybrid host–guest system.

encapsulated in hydrophobic cavities,[18,31] thus enhancing their solubility, while shortening the donor–acceptor distance, and ultimately promoting higher FRET efficiencies.

In the present study, a novel supramolecular structure has been designed, based on the combination of a porphyrinic core with four diethyleneglycol (DEG) spacers terminated with pyrenyl units (**P-Pyr$_4$**). The pyrenyl entities can be encapsulated into prismatic arene–ruthenium metalla-prisms (**Rucage**), in view to increase the water solubility of the pyrenyl-functionalized porphyrin and to avoid aggregation, thus forming a **P-Pyr$_4$@(Rucage)$_4$** hybrid host–guest system (Fig. 1). Electrochemical and photophysical characterization of this system has been performed, with special emphasis on the elucidation of the excited state dynamics using transient absorption spectroscopy. The analysis has been supported by a detailed theoretical investigation that allowed to characterize the interaction among the appended pyrenyl units and the metalla-cages, and the different conformations that the **P-Pyr$_4$@(Rucage)$_4$** system can adopt in solution. The results suggest that in solution the supramolecular structure is retained, and that the metalla-prisms not only increase the solubility and prevent aggregation, but also modify the photophysical behaviour of the pyrenyl-functionalized porphyrin derivative. This study provides new perspectives for supramolecular arene–ruthenium hybrid systems, like energy collection and charge separation applications.

Experimental

General

NMR spectra were recorded on a Bruker Avance Neo Ascend 600 MHz spectrometer. Mass spectra were performed by the ISIC's Mass spectrometry service by nanochip-ESI/LTQ-Orbitrap in positive ion mode.

Synthetic procedures

Panel,[32] **Clip**,[33] **Rucage**,[9] and **P-Pyr$_4$** precursor[34] (see Fig. 2) were prepared according to published methods. Tetraphenylporphyrin (**TPP**), pyrene (**Pyr**), 1-pyrenebutyric acid, silver triflate, 1-ethyl-3-(3-dimethylaminopropyl)carbodiimide (EDCl), 4-dimethylaminopyridine (DMAP) and all other reagents were commercially available and used as received.

P-Pyr$_4$. Under inert conditions, 1-pyrenebutyric acid (451 mg, 1.56 mmol, 6 eq.) and 1-ethyl-3-(3-dimethylaminopropyl)carbodiimide (EDCl) (450 mg, 3.35 mmol, 9 eq.) were dissolved in 15 mL of anhydrous dimethylformamide (DMF). After stirring for 30 min at room temperature, a solution of DEG-porphyrin (342 mg, 0.26 mmol, 1 eq.) and DMAP (318 mg, 2.61 mmol, 10 eq.) in 10 mL of anhydrous DMF was added. The reaction mixture was stirred for 24 h in the dark. Then, the solvent was evaporated under vacuum and the resulting residue was partitioned between dichloromethane (DCM) and a 1 M HCl solution, followed by several water washes. The organic phase was then dried over $MgSO_4$, filtered, and evaporated to dryness. The product was further purified by flash chromatography on a silica column, using a DCM : MeOH gradient up to 9 : 1 (yield 255 mg, 107 μmol, 41%).

^{1}H NMR (600 MHz, $CDCl_3$) δ 8.71 (s, 8H, H$\beta_{pyrrole}$), 8.16 (d, J = 8.3 Hz, 8H, H$_{ph}$), 8.10 (m, 10H, H$_{ph}$ and H$_{pyr}$), 8.09 (s, 2H, H$_{pyr}$), 7.95 (dd, J = 7.6, 1.1 Hz, 4H, H$_{pyr}$), 7.87 (dd, J = 7.7, 1.2 Hz, 4H, H$_{pyr}$), 7.84 (d, J = 7.8 Hz, 4H, H$_{pyr}$), 7.82 (s, 2H, H$_{pyr}$), 7.78 (m, 14H, H$_{pyr}$), 7.65 (d, J = 7.7 Hz, 4H, H$_{pyr}$), 6.99 (t, J = 5.3 Hz, 4H, NHCO$_{porph}$), 6.02 (t, J = 5.5 Hz, 4H, NHCO), 3.74 (dt, J = 21.6, 5.1 Hz, 16H, H$_{DEG}$), 3.65 (m, 16H, H$_{DEG}$), 3.57 (t, J = 5.2 Hz, 8H, H$_{DEG}$), 3.48 (m, 8H, H$_{DEG}$), 3.23 (t, J = 7.7 Hz, 8H, H$_{butyl}$), 2.25 (t, J = 7.3 Hz, 8H, H$_{butyl}$), 2.11 (p, J = 7.5 Hz, 8H, H$_{butyl}$). ^{13}C NMR (151 MHz, $CDCl_3$) δ 172.91 ($COCH_2$), 167.67 (COC$_{ph}$), 145.18 (C$_{ph}$, C$_{porph}$), 135.73 (C$_{porph}$), 134.63

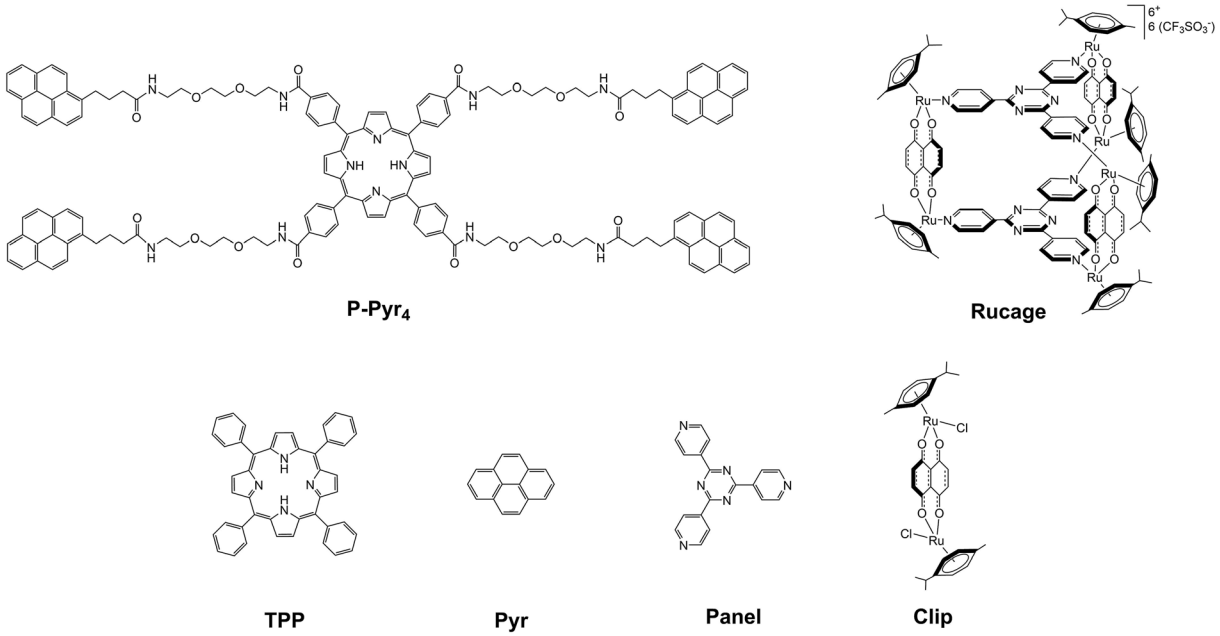

Fig. 2 Molecular structures and codenames of the considered models and building blocks.

(C_{porph}), 133.98 (C_{phCO}), 131.15 (C_{pyr}), 130.63 (C_{pyr}), 129.70 (C_{pyr}), 128.56 (C_{pyr}), 127.28 (CH_{ph}), 127.18 (CH_{ph}), 126.52 (CH_{pyr}), 125.68 (CH_{pyr}), 125.56 (CH_{pyr}), 124.83 (CH_{pyr}), 124.75 (CH_{pyr}), 124.70 (CH_{pyr}), 124.63 (CH_{pyr}), 124.58 (CH_{pyr}), 123.18 (CH_{pyr}), 119.25 ($CH_{\beta pyrrole}$), 70.33 (CH_{2DEG}), 70.31 (CH_{2DEG}), 69.96 (CH_{2DEG}), 69.92 (CH_{2DEG}), 53.55 (DCM), 40.03 (CH_2NH), 39.26 (CH_2NH), 35.99 (CH_2CO), 32.68 (CH_2C_{pyr}), 27.39 ($CH_2CH_2CH_2$). ^{1}H and ^{13}C NMR spectra are reported in Fig. S1 and S2.† UV/Vis (DCM): λ_{max} (ε [M^{-1} cm^{-1}]) = 236 (213 000), 244 (288 000), 267 (121 000), 278 (197 000), 315 (64 000), 329 (126 000), 345 (178 000), 421 (427 000), 517 (20 000), 553 (9000), 592 (6000), 646 (4000). HRMS-ESI *m*/*z*: [**P-Pyr$_4$** + 2Na]$^{2+}$ calcd for $C_{152}H_{142}N_{12}Na_2O_{16}$ 1218.5226; found 1218.5240. [**P-Pyr$_4$** + H + Na]$^{2+}$ calcd for $C_{152}H_{143}N_{12}NaO_{16}$ 1207.5316; found 1207.5330 (see Fig. S5†).

P-Pyr$_4$@(Rucage)$_4$. A mixture of $Ag(CF_3SO_3)$ (71 mg, 275 μmol, 24 eq.) and the **Clip** (100 mg, 137 μmol, 12 eq.) in 25 mL of MeOH was stirred at RT for 4 h. Then, the solution was filtered to remove AgCl, and the **Panel** (29 mg, 92 μmol, 8 eq.) and **P-Pyr$_4$** (28 mg, 12 μmol, 1 eq.) were added. The resulting solution was heated to 80 °C and kept stirring overnight. After evaporation of the solvent, the resulting solid was redissolved in a minimum amount of DCM (1 to 2 mL) and diethyl ether (20 mL) was added dropwise at 0 °C, and left for 4 h to complete precipitation. The product was recovered by filtration, rinsed with diethyl ether and dried under vacuum to give a dark solid (yield 119 mg, 7.27 μmol, 64%). The ^{1}H NMR spectrum in DMSO is reported in Fig. S3.† In addition, a DOSY (diffusion-ordered spectroscopy) NMR analysis was performed (Fig. S4†), showing that the broad signals associated to the host–guest **P-Pyr$_4$@(Rucage)$_4$** system have the same diffusion coefficient, while minor components (**P-Pyr$_4$** and **Rucage**) have faster diffusion coefficients.

Electrochemistry

Cyclic and square wave voltammograms were acquired using a Metrohm Autolab PG-STAT 302 electrochemical workstation controlled by the NOVA 2.0 software. The experiments were conducted in dry DCM (VWR, Uvasol®) solutions containing 0.1 M tetra-*n*-butylammonium hexafluorophosphate (Sigma-Aldrich, electrochemical grade) and approximately 2×10^{-4} M analyte, under a dry nitrogen atmosphere, at a scan rate of ν = 100 mV s^{-1}. The experimental setup involved a single-compartment three-electrode cell fitted with platinum wire counter and pseudo-reference electrodes, along with a glassy carbon working electrode (BioLogic). All recorded redox potentials are referenced to the ferrocene/ferrocenium (Fc/Fc^+) redox couple, which was added at the conclusion of each experiment, serving as an internal reference system.

Absorption and emission spectroscopy, photophysics

Spectroscopic grade DCM (Merck, Uvasol®) was passed through an alumina column to remove traces of acid. **TPP** was purchased from Porphychem, α-NPO (2-(1-naphthyl)-5-phenyloxazole) from Lambdaphysik and **Pyr** from Acros.

Absorption spectra were recorded with a Perkin–Elmer Lambda 650 UV-Vis or a Lambda 950 UV-Vis-NIR spectrophotometer in 1 cm quartz cuvettes. Emission spectra were collected with an Edinburgh FLS920 spectrofluorometer, equipped with a Peltier-cooled Hamamatsu R928 PMT (280–850 nm). The spectra have been corrected for the wavelength-dependent phototube response. Measurements in the NIR region were performed with a FLS920 fluorimeter (Edinburgh) equipped with a Hamamatsu R5509-72 InP/InGaAs phototube multiplier supercooled at 193 K in a liquid

nitrogen cooled housing, and a TM300 emission monochromator with a NIR grating blazed at 1000 nm (sensitivity range: 400–1700 nm).

Fluorescence quantum yields were evaluated with the comparative method developed by Demas and Crosby,[35] by correcting the spectra for the wavelength-dependent photomultiplier response. The standards used were α-NPO in aerated cyclohexane (ϕ_{fl} = 0.94)[36] for the pyrene unit and **TPP** in toluene (ϕ_{fl} = 0.11)[37] for the porphyrin component. Measurements at 77 K were performed using Pyrex tubes dipped in liquid nitrogen in a quartz Dewar. Excitation spectra were corrected for the wavelength-dependent lamp intensity.

Excited state lifetimes in the nanosecond range were determined by using an IBH time-correlated single-photon counting apparatus with nanoLED excitation sources at 331 nm and 465 nm.

Pump–probe transient absorption measurements were performed with an Ultrafast Systems HELIOS (HE-VIS-NIR) femtosecond transient absorption spectrometer by using, as excitation source, a Newport Spectra Physics Solstice-F-1K-230 V laser system, combined with a TOPAS Prime (TPR-TOPAS-F) optical parametric amplifier (pulse width: 100 fs, 1 kHz repetition rate) tuned at 420 nm and 700 nm. The pump energy on the sample was 1 μJ per pulse or 10 μJ per pulse, respectively. Excitation at 420 nm required a 10 times reduction of the laser power due to the photoinstability of the porphyrin components upon excitation with high energy photons, leading to weak transient signals. The overall time resolution of the system is 300 fs. Air-equilibrated solutions in 0.2 cm optical path cells were analysed under continuous stirring. The Surface Xplorer V4 software from Ultrafast Systems was used for data acquisition and analysis. The 3D data surfaces were corrected for the chirp of the probe pulse prior to analysis.

Estimated errors are 10% on transient absorbance lifetimes, 10% for luminescence lifetimes, 10% for molar absorption coefficients and 10% on quantum yields.

Modelling

Different computational approaches have been employed to analyse a series of molecular **P-Pyr$_4$@(Rucage)$_4$** models in order to aid the interpretation of the experimental results. The simplest models, which consist of **Pyr** and modified **Clip** (**Clip-2**, where Cl is replaced with pyridine moieties, see Fig. S6†), were subjected to density functional theory calculations (DFT). Geometry optimizations were performed using range-separated hybrid functionals (LC-PBE functional),[38] with a Def2-SVP basis set[39,40] for all atoms, with relative effective core potentials for Ru atoms. Recognizing the significant influence of solvation parameters, environmental effects (*i.e.*, DCM) were incorporated using a conductor-like polarizable continuum model (CPCM).[41] The directions and intensities of the dipole moments were determined for **Pyr**, while the transition electric dipole moments for modified **Clip** were obtained through time-dependent DFT calculations (TD-DFT),[42,43] which were conducted at the same level of theory as used for geometry optimizations. All DFT and TD-DFT calculations were performed using ORCA 5.0.4 software.[44]

Complex models were analysed using the advanced GFN2-xTB method,[45] implemented into the xTB software,[45–47] to overcome the limitations associated with DFT calculations. This method is primarily designed for the rapid, robust, and reasonably accurate computation of large molecules, comprising more than 1000 atoms, while maintaining a good accuracy performance and computational cost for the target properties.[48] Geometry optimization was conducted with very tight convergence criteria for energies and gradients (E_{conv} = 1 × 10^{-7} Eh; G_{conv} = 2 × 10^{-4} Eh α^{-1}). Implicit solvent effects (*i.e.*, DCM) were incorporated by employing the Analytical Linearized Poisson–Boltzmann (ALPB) method.[49]

For **P-Pyr$_4$@(Rucage)$_4$**, six different conformers were generated: the first two exhibit linear conformation of the branches alternatively below and above the porphyrin plane (**P-Pyr$_4$@(Rucage)$_4$**_I) or along the plane (**P-Pyr$_4$@(Rucage)$_4$**_II). In the remaining models, the conformations of the branches were progressively modified (from 1 to 4 branches, labelled **P-Pyr$_4$@(Rucage)$_4$**_III, **P-Pyr$_4$@(Rucage)$_4$**_IV, **P-Pyr$_4$@(Rucage)$_4$**_V, **P-Pyr$_4$@(Rucage)$_4$**_VI) to enable interactions between the porphyrin core and the cages. A simplified mono-functionalised system, labelled **P-Pyr@(Rucage)** was used to study the inclusion of **Pyr** inside the **Rucage**, using relaxed scan calculations (Fig. S19†). Triflate anions were kept as the counterions and placed in proximity of the **Rucage** to neutralize its +6 positive charge; indeed, preliminary calculations suggested that the positively charged models were unstable without proper neutralization.

The dissociation energy (*De*), the interaction energy (*IE*) and the deformation energy (*Def*)[50,51] were obtained as reported in eqn (1).

$$De = |IE| - Def \quad (1)$$

The *De* is defined in eqn (2):

$$De = \left(E_{\text{relax\_P-Pyr}_4} + 4E_{\text{relax\_Rucage}}\right) - E_{\text{P-Pyr}_4\text{@(RuCage)}_4} \quad (2)$$

where $E_{\text{P-Pyr}_4\text{@(Rucage)}_4}$ is the total energy for the **P-Pyr$_4$@(Rucage)$_4$** complex and $E_{\text{relax\_P-Pyr}_4}$ and $E_{\text{relax\_Rucage}}$ are the energies of the relaxed **P-Pyr$_4$** and **Rucage** molecules, respectively. *De* can be decomposed in *IE* and *Def*; *IE* is similar to *De* but calculated between fragments in the structures they have in the complexes (eqn (3)):

$$IE = E_{\text{P-Pyr}_4\text{@(RuCage)}_4} - \left(E_{\text{P-Pyr}_4} + 4E_{\text{Rucage}}\right) \quad (3)$$

where $E_{\text{P-Pyr}_4}$ and E_{Rucage} are the energies of isolated molecules at the coordinate of the complex. For convenience, the absolute value of *IE*, |*IE*|, was discussed in this work, since a large absolute value of *IE* is associated with a high stabilizing interaction energy.

Def evaluates the energy cost to bring each fragment from its optimized structure as an isolated species to that in the complex (eqn (4)) and quantitatively describes the structural deformations of the molecules.

$$Def_{\text{P-Pyr}_4} = E_{\text{relax\_P-Pyr}_4} - E_{\text{P-Pyr}_4} \quad (4)$$

Energy transfer

In the context of a general energy transfer process, one can derive the intramolecular rate constant from either eqn (5) or (6):

$$k_{EnT} = \frac{1}{\tau_q} - \frac{1}{\tau_0} \quad (5)$$

$$k_{EnT} = \frac{1}{\tau_q}\left(\frac{\phi_0}{\phi_q} - 1\right) \quad (6)$$

Here, τ_q and ϕ_q represent the lifetime and quantum yield of the donor quenched emission, while τ_0 and ϕ_0 are associated with the donor unquenched lifetime and quantum yield, respectively.

The overall efficiency of the intramolecular energy transfer process can be assessed using eqn (7):

$$\eta_{EnT} = \frac{k_{EnT}}{k_{EnT} + k_{in}} \quad (7)$$

In this equation, $k_{in} = 1/\tau_0$ signifies the intrinsic deactivation rate constant of the unquenched donor luminophore, with k_{EnT} defined earlier.

The calculation of the interchromophoric distance-dependent energy transfer rates, grounded in the Förster theory, involves the following eqn (8)–(10):

$$k_F(d) = \frac{1}{\tau_0}\left(\frac{R_0}{r}\right)^6 \quad (8)$$

$$k_F = \frac{8.79 \times 10^{-25}\kappa^2\phi_0}{n^4\tau_0 r} J_F \quad (9)$$

$$J_F = \int_0^\infty F_D(\lambda)\varepsilon_A(\lambda)\lambda^4 d\lambda \quad (10)$$

Here, r represents the donor–acceptor interchromophoric distance, R_0 is the Förster critical distance, κ^2 denotes the orientation factor, n stands for the refractive index of the solvent, J_F is the overlap integral, $F_D(\lambda)$ is the normalized corrected fluorescence intensity of the donor, $\varepsilon_A(\lambda)$ is the absorption coefficient of the acceptor, and λ signifies the wavelength.[52]

Results and discussion

Synthetic procedures

The tetrapyrenylporphyrin derivative (**P-Pyr$_4$**) was obtained in good yield from 1-pyrenebutyric acid and the corresponding tetrapegylated amido-porphyrin (Scheme 1). Upon formation of **P-Pyr$_4$**, new signals associated to the pyrenyl protons were observed in the ^{1}H NMR spectrum, especially those of the pyrenyl aromatic protons between 7.6 and 8.1 ppm (Fig. S1†). Under electrospray condition **P-Pyr$_4$** shows in the mass spectrum a dicationic peak at m/z = 1196.5420, in agreement with a di-protonated compound $[M + 2\ H^+]^{2+}$ (Fig. S5†).

Then, **P-Pyr$_4$** was added during the synthesis of the arene ruthenium metalla-prisms, thus allowing the formation of the tetra-encapsulated system **P-Pyr$_4$@(Rucage)$_4$** to take place. This final assembly was performed in methanol, to force the pyrenyl units to hide inside the hydrophobic cavity of the metalla-prism, $[(\eta^6\text{-}p\text{-cymene})_6Ru_6(\mu\text{-dioxidonaphthoquinonato})_3(tpt)_2]^{6+}$ (**Rucage**). Therefore, **P-Pyr$_4$@(Rucage)$_4$** is cationic with an overall charge of 24+, and the product isolated as a salt, with triflate counter ions, is **[P-Pyr$_4$@(Rucage)$_4$]**$(CF_3SO_3)_{24}$. In solution,

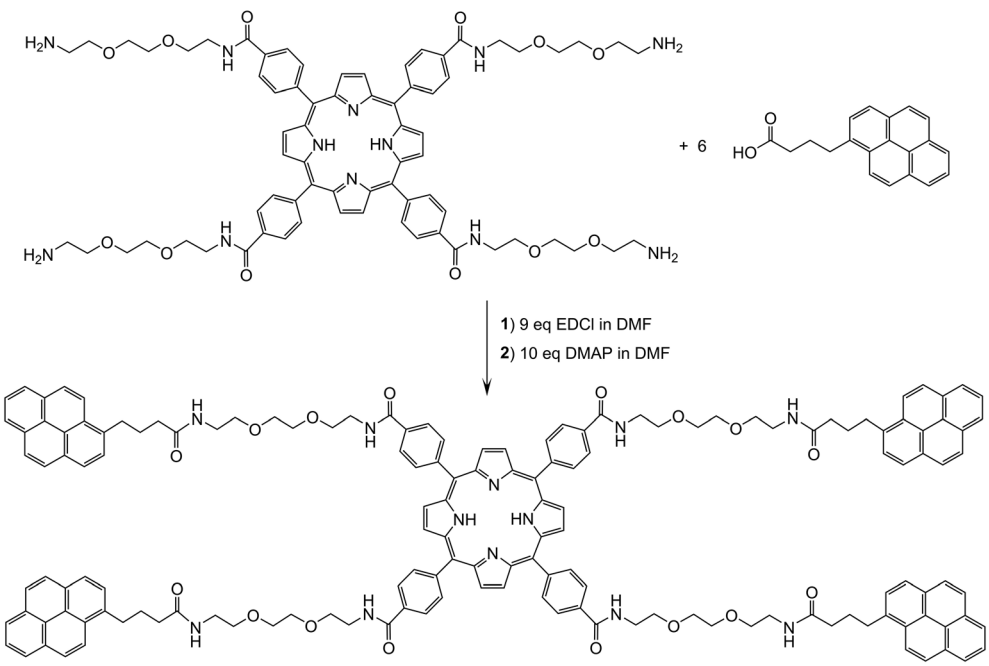

Scheme 1 Synthesis of **P-Pyr$_4$** from 1-pyrenebutyric acid and the DEG-porphyrin precursor.

dynamic exchange between the host and the guest cannot be totally ruled out, as the binding constant for such 1 : 1 pyrenyl-functionalized derivatives and arene ruthenium metalla-prisms has been estimated to be around 7.5×10^4 M^{-1} in acetonitrile.[53] However, in the range of concentrations used, we can assume that an intact **P-Pyr$_4$@(Rucage)$_4$** system is predominant, as suggested by the ^{1}H NMR spectrum of **P-Pyr$_4$@(Rucage)$_4$** (Fig. S3†), showing an intense broadening of the pyrenyl signals.

Electrochemistry

In order to investigate the possibility of redox reactions within the units of the studied systems, the electrochemical characterization of **Rucage** and its models **Clip** and **Panel** has been performed in DCM with tetrabutylammonium hexafluorophosphate supporting electrolyte (0.1 M). Ferrocene was used as internal reference.

The cyclic voltammogram and square-wave voltammogram of **Rucage** are shown in Fig. 3, while those of **Panel** and **Clip** are displayed in Fig. S7 and S8.† The electrochemical data are collected in Table 1. **Panel** shows three reversible reduction waves (Fig. S7†), that can be attributed to the reduction of the three pyridine rings of the molecule.[54] Conversely, **Clip** presents two reduction and two oxidation waves (Fig. S8†), all the processes being quasi-reversible. These waves correspond to oxidation of the Ru centres and reduction of the organic naphthoquinonato ligands, respectively. With regard to **Rucage**, a complex behaviour is observed (Fig. 3): four reduction and two quasi-reversible oxidation waves are detected. By comparison with the data of the models, two of the four reduction processes, *i.e.* $E^{3-4}_{red,\mathbf{Rucage}}$ (see Table 1), can be ascribed to the reduction of the panels, with the potentials slightly negatively shifted with respect to the model (Table 1). The reduction wave $E^{1}_{red,\mathbf{Rucage}}$ at −0.91 V likely corresponds to the first reduction of the organic ligand of a Ru clip, largely positively shifted with respect to the model ($E^{1}_{red,\mathbf{Clip}}$ = −1.32 V, Table 1). The reduction process $E^{2}_{red,\mathbf{Rucage}}$ at −1.44 V can reasonably originate from the merging of two independent redox processes, namely, the second reduction of the **Clip** positively shifted (Table 1), and the first reduction of the **Panel**. Eventually, the two oxidation processes, $E^{1-2}_{ox,\mathbf{Rucage}}$, originate from the oxidation of the metal centres of the clips. Also in this case, the potentials are positively shifted with respect to **Clip** alone, with the first oxidation peak particularly affected. These positive shifts are likely due to the increase of the residual positive charge on the Ru atoms induced by the coordination of the pyridine moieties of the **Panel**, as indicated by the calculation of the Mulliken charges. Indeed, in the **Clip** the two Ru atoms show similar negative Mulliken charge values (≈−0.21), while in the **Clip-2** model (where pyridine moieties replace the Cl atoms) an increase in the Mulliken charge values up to −0.08 is observed.

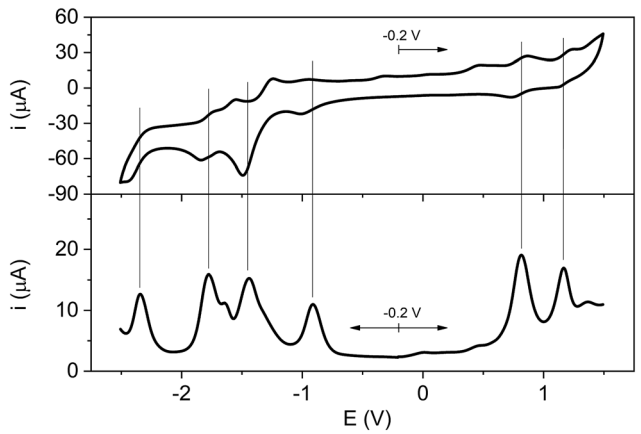

Fig. 3 Cyclic (top panel) and square wave (bottom panel) voltammetry scans of **Rucage** in DCM solution. CV anodic scan starting from −0.2 V; SWV anodic and cathodic scans from −0.2 V (the sign of the cathodic current is reversed).

Table 1 Electrochemical data for **Rucage** and models (**Panel** and **Clip**) in DCM[a]

	E^4_{red}	E^3_{red}	E^2_{red}	E^1_{red}	E^1_{ox}	E^2_{ox}
Panel	—	−2.24	−1.76	−1.34	—	—
Clip	—	—	−1.60	−1.32	0.42	0.90
Rucage	−2.34	−1.78	−1.44	−0.91	0.81	1.17

[a] Potentials (in Volts) reported *vs.* Fc/Fc^+, determined by the peaks of the square wave voltammograms.

Photophysical characterization of P-Pyr$_4$@(Rucage)$_4$

The photophysical characterization of the supramolecular system **P-Pyr$_4$@(Rucage)$_4$** and all models has been performed in DCM. Due to the complexity of the system, two sets of models have been considered: (i) **P-Pyr$_4$** and **Rucage** as first level components and (ii) their further constituents, *i.e.*, tetraphenyl porphyrin (**TPP**) and pyrene (**Pyr**) as models for **P-Pyr$_4$**, and **Panel** and **Clip** as models for **Rucage** (Fig. 2).

Comparison of the absorption spectra of **P-Pyr$_4$** and **Rucage** with those of their respective models and their weighted sum is reported in Fig. S9 and S10.† In case of **P-Pyr$_4$**, the spectrum of the array well matches the porphyrin features in the region 350–700 nm, where only a slight decrease and broadening of the Soret band are observed, while the bands of the pyrenyl units appear red-shifted by 5–8 nm (Fig. S9†). These results indicate the presence of weak electronic interactions between the different units in the array. Conversely, comparison of the spectrum of **Rucage** with the sum of the spectra of the models shows large differences (Fig. S10†), indicating strong electronic interactions among the units in the cage. It can be noticed that the cage, as well as the **Clip** component, presents absorption features up to 800 nm.

The absorption spectrum of **P-Pyr$_4$@(Rucage)$_4$** is shown in Fig. 4, together with those of its components, **P-Pyr$_4$** and **Rucage**, and their weighted sum. The spectrum reasonably matches the sum of the spectra of the components, with a clear decrease only in the Soret region and in the pyrene peaks. These data indicate the presence of ground state inter-

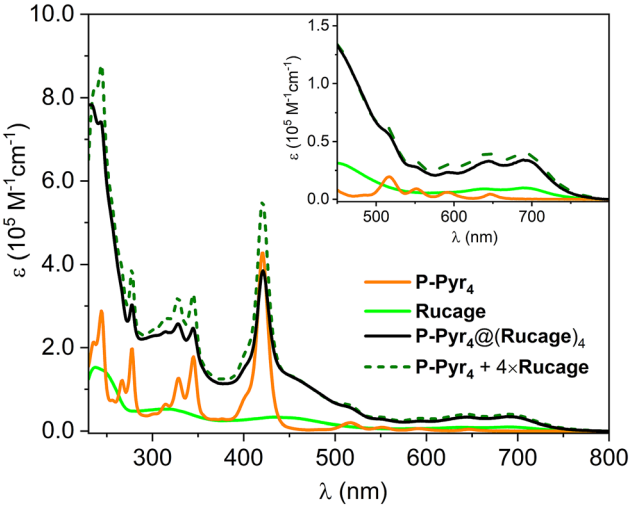

Fig. 4 Absorption spectra of **P-Pyr$_4$@(Rucage)$_4$** and its respective models **P-Pyr$_4$** and **Rucage** in DCM. The weighted sum of the spectra of the models is also reported. Inset: magnification of the 450–800 nm region.

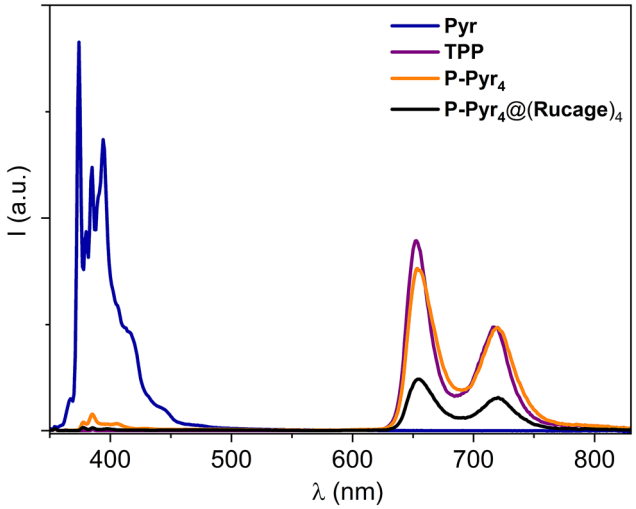

Fig. 5 Corrected emission spectra of isoabsorbing solutions of **P-Pyr$_4$**, **P-Pyr$_4$@(Rucage)$_4$** and models **Pyr** and **TPP** in DCM; excitation at 345 nm (A_{345} = 0.11); at this wavelength the pyrenyl units are almost exclusively excited (90% of the absorbed photons).

actions among the cages and the other units of the supramolecular system.

Rucage and its components were found to be non-emissive both at room temperature and at 77 K, even probing the NIR spectral range up to 1400 nm. Also, selective excitation of the Ru component at 700 nm in **P-Pyr$_4$@(Rucage)$_4$** resulted in no appreciable emission at both temperatures.

On the other hand, the porphyrin component in **P-Pyr$_4$** displays typical porphyrin fluorescence, when selectively excited at 515 nm, with a quantum yield of 0.10 and a lifetime of 9.2 ns (Table 2 and Fig. S11†). Interestingly, the fluorescence of the pyrenyl units in **P-Pyr$_4$** is almost completely quenched, as observed upon their excitation at 345 nm (Fig. 5). It is evident that this quenching is accompanied by the full sensitization of the porphyrin emission, that appears comparable to that of the **TPP** model (Fig. 5). These results point to a very efficient energy transfer from the pyrene moieties to the central porphyrin core in **P-Pyr$_4$** (*vide infra*).

Selective excitation of the pyrene components in **P-Pyr$_4$@(Rucage)$_4$** leads again to the complete quenching of their fluorescence in the array, but, in this case, the quenching is accompanied by only a 30% recovery of the porphyrin emission (Fig. 5). Indeed, the yield estimated for the porphyrin fluorescence in **P-Pyr$_4$@(Rucage)$_4$** upon excitation at 515 nm is one third of that of **TPP** (Table 2 and Fig. S11†). Quenching of the porphyrin fluorescence in **P-Pyr$_4$@(Rucage)$_4$** is attested also by lifetime measurements, which reveal the presence of a short component of 400 ps in addition to the value of *ca.* 9 ns of the unquenched porphyrin component (Table 2). It can be thus inferred that, in **P-Pyr$_4$@(Rucage)$_4$**, an efficient energy transfer from the pyrene to the porphyrin units is still operative, but the sensitized porphyrin singlet is partially depopulated by processes involving the cage components.

Further confirmations that an effective **Pyr →Porph** energy transfer occur in both arrays comes from different experiments. The excitation spectra of **P-Pyr$_4$** and **P-Pyr$_4$@(Rucage)$_4$**, collected at 720 nm, where only emission from the porphyrin is present, well match the absorption spectrum of **P-Pyr$_4$** in both porphyrin and pyrenyl domains (Fig. S12†). Also, upon excitation of the pyrene component at 331 nm, a lifetime of *ca.* 370 ps was measured at 380 nm in both **P-Pyr$_4$** and **P-Pyr$_4$@(Rucage)$_4$** (Fig. S13† and Table 2), corresponding to the quenched pyrene lifetime, accompanied by a rise of porphyrin emission in the 650–750 nm range with the same time constant (Fig. S13†), attesting the sensitization of the porphyrin singlet. A detailed analysis of the **Pyr →Porph** energy transfer process is discussed later on in the Energy transfer section.

Table 2 Luminescence data at room temperature for arrays **P-Pyr$_4$** and **P-Pyr$_4$@(Rucage)$_4$** and models **Pyr** and **TPP** in DCM

		λ_{max}[a] (nm)	ϕ_{fl}[b]	τ[e] (ns)
Pyr[f]		374, 385, 394	0.063[c]	26.3
TPP		652, 718	0.091[d]	8.1
P-Pyr$_4$	^{1}**Pyr**	378, 385, 405	*ca.* 1.0×10^{-3}	0.37
	^{1}**Porph**	654, 720	0.10[d]	9.2
P-Pyr$_4$@(Rucage)$_4$	^{1}**Pyr**	378, 385, 398	*ca.* 1.0×10^{-3}	0.36
	^{1}**Porph**	654, 720	0.030[d]	0.40 (70%); 9.1 (30%)[g]

[a] Emission maxima from corrected spectra. [b] Fluorescence quantum yields. [c] Measured with reference to α-NPO in aerated cyclohexane (ϕ_{fl} = 0.94),[36] excitation at 321 nm. [d] Porphyrin emission quantum yield, measured with reference to **TPP** in aerated toluene (ϕ_{fl} = 0.11),[37] excitation at 515 nm. [e] Excited state lifetimes measured with the single photon counting technique, excitation at 465 nm for the porphyrin component and 331 nm for pyrene (in brackets: percentages of pre-exponential values). [f] Data in line with those reported in ref. 10. [g] Lifetimes measured with single photon counting technique. An ultrafast component is also identified in **P-Pyr$_4$@(Rucage)$_4$** by means of transient absorption analysis (see Discussion).

In order to shed light on the photoinduced processes at the basis of the observed porphyrin quenching in **P-Pyr$_4$@(Rucage)$_4$**, transient absorption measurements with femtosecond resolution have been performed. Two excitation wavelengths have been selected: 700 nm, where only the cage components absorb, and 420 nm, where the porphyrin components are prevalently excited (see Fig. 4).

Excitation at 700 nm of **P-Pyr$_4$@(Rucage)$_4$** leads to the observation of an intense absorption band at 570 nm, with a broad tail extending in the NIR region and ground state bleaching features below 470 nm (Fig. 6). The kinetics is represented by a bi-exponential function all over the entire spectral range: a short decay of *ca.* 10 ps dominates the evolution in the visible region, paralleled by a rise of a band in the 900–1200 nm range, while the second process is represented by a decay of 2.5 ns. The observed behaviour can be tentatively interpreted as follows: (i) an initial fast process (10 ps) leads to the population of the lowest MLCT triplet state of the Ru cage component, whose spectrum is characterized by bands at *ca.* 540 nm and at *ca.* 1020 nm. This process can be ascribed to solvent induced vibrational relaxation of the triplet state, being intersystem crossing an ultrafast process; (ii) the formed triplet then decays on a longer time scale (2.5 ns). These features are very similar to those observed upon excitation of **Rucage** at 700 nm (Fig. S14†), indicating that the photophysics of the cage is not affected by the presence of the pyrenyl unit inside its cavity. By looking at the behaviour of model **Clip**, upon excitation at the same wavelength, a quite similar scenario is observed (Fig. S15†), with the difference of red-shifted spectra (maxima at 620 nm for the end-of-pulse spectrum and 640 and 1080 nm for the triplet state) and faster kinetics (*ca.* 5 ps and 400 ps) with respect to the cage system. The slower kinetics observed in the latter can be attributed to the presence of the panel ligands, whose orbitals might be involved in the charge-transfer transitions.

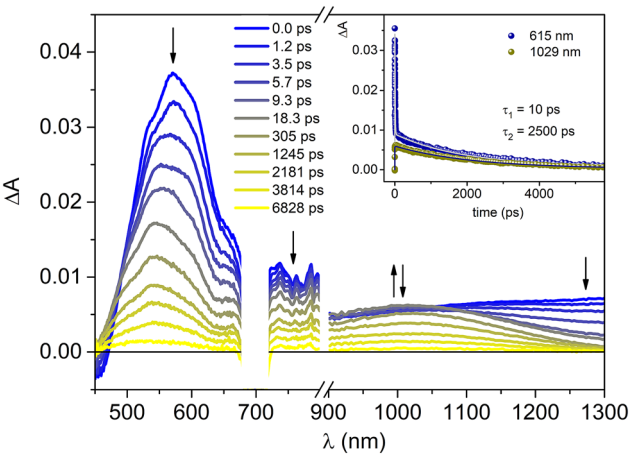

Fig. 6 Transient absorption spectra of **P-Pyr$_4$@(Rucage)$_4$** in DCM at different delays. Excitation at 700 nm (A_{700} = 0.34, 0.2 cm optical path, 10 μJ per pulse). Inset: ΔA time evolutions (dots) and fittings (lines) at the indicated wavelengths.

Upon excitation at 420 nm, the end-of-pulse spectrum observed for the array **P-Pyr$_4$@(Rucage)$_4$** (Fig. 7a) is different from that of **P-Pyr$_4$** (Fig. 7b), the latter presenting usual features of porphyrinic systems with positive absorption in the visible region overlaid with ground state bleaching of the Q-bands, stimulated emission at 654 and 720 nm and a positive band in the NIR region at 1080 nm. In **P-Pyr$_4$@(Rucage)$_4$**, indeed, the spectrum shows a more pronounced absorption in the 550–650 nm region. However, the most important difference resides in the kinetics: while for **P-Pyr$_4$** a slow decay of the signal is observed (Fig. 7b, inset), compatible with a lifetime of 9.2 ns as measured from fluorescence analysis (which is outside the maximum timescale of the transient instrumentation), in **P-Pyr$_4$@(Rucage)$_4$** a more complex scenario is detected, with multi-exponential decays that include short components (Fig. 7a, inset). To get further insights in the comprehension of the transient data, a global fit analysis has been performed on the visible region of the matrix. Fig. S16† shows the spectral distribution of the amplitudes of the calculated lifetimes.[55] A lifetime of 15 ps is associated to a spectrum with bands between 550 and 650 nm, indicative of a free-base porphyrin cation,[56,57] while a component of 400 ps (fixed in the analysis) is associated to a typical spectrum of a porphyrin singlet. The spectrum corresponding to a lifetime of *ca.* 5 ns is similar to that of **Rucage**. As a confirmation, the transient absorption of **Rucage** excited at the same wavelength is reported in Fig. S17:† it can be observed that it reproduces well what observed upon excitation at 700 nm (Fig. 6), both in spectral features and decay lifetimes. The decay of 5 ns detected in the complex can thus be ascribed to the **Rucage** triplet (the longer lifetime with respect to that of the empty cage can derive from a rigidification of the system once hosting the pyrene moiety). Finally, a spectrum with an "infinite" lifetime on the timescale of the instrument matches the typical spectrum of a porphyrin triplet.[58]

On the basis of these indications a plausible description of the processes occurring in **P-Pyr$_4$@(Rucage)$_4$** can be drawn. Different conformations of the array can exist in solution due to the flexibility of the pegylated branches, as supported by GFN2-xTB calculations (see the Modelling section below). This leads to different distances between the porphyrin core and the metalla-prisms that can affect the photophysics of the system.

Conformations where one to four branches are folded towards the porphyrin core (**P-Pyr$_4$@(Rucage)$_4$**_III–VI) are more stable in solution than those where the branches are open in an extended "star" shape (**P-Pyr$_4$@(Rucage)$_4$**_I–II). Distances in the order of 5–6 Å between the porphyrin and the metallacages in these conformations are found, considering the minimum distances among the centre of the porphyrin and the centre of the naphtoquinonato moiety of the **Clip** (Table S5†) or among the centre of the porphyrin and the Ru atoms (Table S6†). These short distances allow for an ultrafast deactivation of the porphyrin singlet by electron transfer towards the cage. The energy of the charge separated (CS) state Porph$^+$–Rucage$^-$ can be estimated as 1.43 eV, by considering

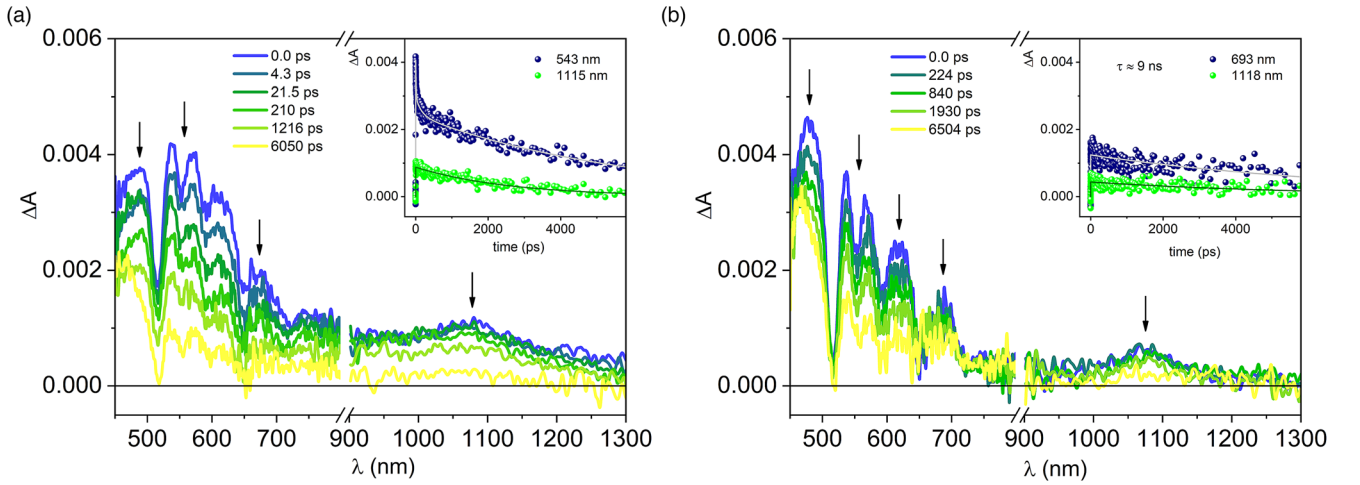

Fig. 7 Transient absorption spectra of **P-Pyr$_4$@(Rucage)$_4$** (a) and **P-Pyr$_4$** (b) in DCM at different delays. Excitation at 420 nm (A_{420} = 0.20, 0.2 cm optical path, 1 μJ per pulse). Inset: ΔA time evolutions (dots) and fittings (lines) at the indicated wavelengths.

the measured reduction potential of the **Rucage** (−0.91 V *vs.* Fc^+/Fc, Table 1) and the oxidation potential of **TPP** (+0.52 V in DCM, *vs.* Fc^+/Fc).[59] Population of the CS state from the porphyrin singlet is thus thermodynamically allowed (Scheme 2). On these arguments, the detection, at the end-of pulse, of the formed $Porph^+$ species can be explained (the features of the reduced **Rucage** are not clearly observable). The lifetime of this CS state is thus in the order of 15 ps.

Accordingly, in conformations where the distance between the porphyrin and the metalla-prisms is higher, in the order of 13–16 Å (see below), the decay of the porphyrin singlet occurs in the order of hundreds of ps, corresponding to the measured 400 ps in the fluorescence decay (Table 2).[60] This deactivation can be ascribed to energy transfer towards the cage components (as discussed in the Energy transfer section); the **Rucage** triplet that forms then decays in 5 ns.

Finally, the last species that can be identified from the transient analysis on long time scales is the porphyrin triplet. Its population can derive both by charge recombination (the CS state and the porphyrin triplet are almost isoenergetic, Scheme 2) or by intersystem crossing in the fraction of the porphyrin population that is not quenched by photoinduced reactions. The latter condition is observed in conformations where the porphyrin and the cage are too far from each other to enable any photoinduced process among them, as for **P-Pyr$_4$@(Rucage)$_4$**_I–II (average distance of the order of 24–25 Å, see below), and is confirmed by the lifetime of 9.1 ns detected with fluorescence analysis (Table 2).

In order to get further information on the energy transfer dynamics between the triplet states of the porphyrin and the cage components in **Pyr$_4$@(Rucage)$_4$**, the production of singlet oxygen from optically matched solutions of **TPP**, **P-Pyr$_4$**, **Rucage** and **P-Pyr$_4$@(Rucage)$_4$** has been measured. Excitation has been performed at 400 nm, where the porphyrin unit is selectively excited in **P-Pyr$_4$** and is absorbing 50% of the light in **P-Pyr$_4$@(Rucage)$_4$**. With respect to **TPP**, taken as standard (ϕ_Δ = 0.60 in DCM),[62] the yield is only slightly lower for **P-Pyr$_4$** (ϕ_Δ = 0.55) while it is reduced to ϕ_Δ = 0.08 in **Pyr$_4$@(Rucage)$_4$** (Fig. S18†). The latter corresponds to the yield of formation of the porphyrin triplet in the array, by considering a 50% absorption of the porphyrin in the array and a 70% quenching of the porphyrin singlet. This result rules out the occurrence of an energy transfer from the porphyrin triplet to the cage triplet, while a singlet–singlet energy transfer is possible (a detailed analysis is reported in the Energy transfer section). It can be also noticed that for **Rucage** the singlet oxygen signal is not detected.[63] This results can be attributed either to a non-effective encounter of the cage with molecular oxygen, due to the short triplet lifetime, or to a lower energy of the cage triplet with respect to that of singlet oxygen (0.98 eV).

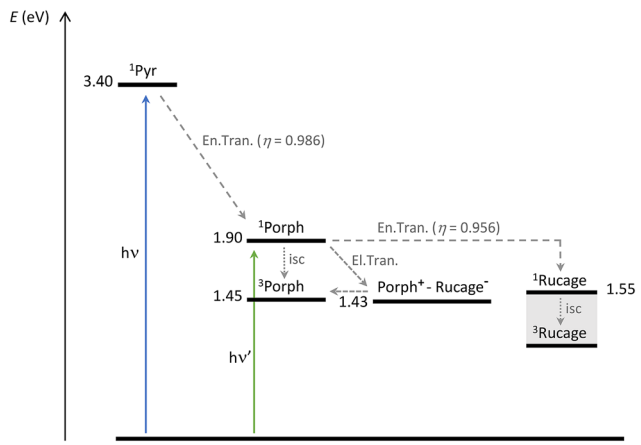

Scheme 2 Energy level diagram and photoinduced processes for the system **P-Pyr$_4$@(Rucage)$_4$**. Singlet and triplet energy levels for the pyrene and porphyrin components are derived from data of the present paper and from the literature.[61] The singlet energy level of **Rucage** has been estimated as onset of the absorption spectrum, while the triplet level could not be estimated and its position in the scheme is qualitative. The energy of the CS state $Porph^+$–$Rucage^-$ has been calculated as described in the text.

Modelling

Computational calculations were employed to support the interpretation of experimental findings. Initially, DFT and TD-DFT calculations were applied to **Pyr** and modified **Clip-2** models to obtain electric dipole and transient electric dipole moments, which were further used for the energy transfer calculations. The ground state optimized structure of **Pyr** shows an electric dipole moment of 3×10^{-4} D, oriented on the plane of the carbon atoms, as reported in Fig. S20a.† In the modified **Clip-2** the electric transition dipole moment of 6.6 D, calculated between the ground state and the first excited S_1 state, is located in the middle of the aromatic rings of the dihydroxynaphthoquinonato moiety, and is parallel to it (Fig. S20b, c†).

The GFN2-xTB method has been initially used to investigate the encapsulation of **Pyr** in **Rucage** by relaxed scan calculations. The obtained energy profile (ΔE) is reported in Fig. S21.† At the starting point, **P-Pyr** is placed at 45.5 Å from the **Rucage** and no interaction is observed from the zero value of ΔE. A decrease in ΔE is detected approximately at 23 Å, with a value of −8.6 kcal mol^{-1}, indicating that the first interaction between the **P-Pyr** pegylated branch and the **Rucage** is taking place, while the **Pyr** is involved in an intramolecular interaction. Then, a stronger decrease in the ΔE value is observed (from −8.6 to −31.0 kcal mol^{-1}) in the range 15.0–6.5 Å, due to the progressive inclusion of the **Pyr** moiety inside the **Rucage** (Fig. S21†). In the last part of the curve, negligible decrease in ΔE is reported with an energy minimum of −34.1 kcal mol^{-1} when the two entities are *ca.* 3.0 Å apart. The quantitative study of the **Porph**/**Pyr**/**Rucage** interaction has been completed with a qualitative analysis performed by Independent Gradient Model (IGM) method.[64,65] IGM analysis (Fig. S22†) demonstrates the presence of π–π stacking, CH–π and CH–O interactions, all contributing to the stabilisation of the supramolecular system.

To investigate the stability of various **P-Pyr$_4$@(Rucage)$_4$** conformations, six conformers were examined (Fig. 8), and the results are reported in Table 3 (refer also to Tables S1 and S2†). All investigated models exhibit highly positive *De* values, indicating the establishment of stable interactions between **P-Pyr$_4$** and four **Rucage** assemblies. As depicted in Table 3, *De* values increase with the increasing number of **Rucage** molecules interacting with the **P-Pyr$_4$** moiety. A similar trend is observed in $|IE|$ and *Def* values and their individual components (Tables S1 and S2†), corresponding to an increasing number of interactions between **Rucage** and **P-Pyr$_4$**, with a consequent increase in the deformation of the systems (Fig. S23†).

The first two models exhibit a linear conformation of the branches. **P-Pyr$_4$@(Rucage)$_4$_I**, with branches oriented below and above the porphyrin plane, is found to be less stable compared to **P-Pyr$_4$@(Rucage)$_4$_II** (Table 3), where branches are positioned parallel to the porphyrin plane. These differences in stability can be attributed to the interactions between two **Rucage** units and the interspersed triflate anions in **P-Pyr$_4$@(Rucage)$_4$_II** (Fig. S24†). The $|IE|$ decomposition, as reported in Table S1,† reveals similar values for both systems, ranging between 41.6 and 56.4 kcal mol^{-1}, indicating different interactions between **Rucage** and the **P-Pyr$_4$** branches (Fig. 8), with a centre of porphyrin – centre of naphtoquinonato pillar average distance ($d_{\text{Porph–Rucage}}$, Table S5†) of 24.7 Å for **P-Pyr$_4$@(Rucage)$_4$_I** and 24.1 Å for **P-Pyr$_4$@(Rucage)$_4$_II**.

In **P-Pyr$_4$@(Rucage)$_4$_III** one of the branches undergoes self-folding, facilitated by the interaction between **Rucage** and the porphyrin core (Fig. 8), resulting in a minimum $d_{\text{Porph–Rucage}}$ distance of 5.7 Å (**Porph-Ruc$_1$** in Table S5†). This interaction leads to a *De* stabilization of approximately 23 kcal mol^{-1} compared to **P-Pyr$_4$@(Rucage)$_4$_II** (Table 3). Indeed, the decomposition of $|IE|$ reveals a significant increase, rising from 56.4 kcal mol^{-1} in **P-Pyr$_4$@(Rucage)$_4$_II** to 74.6 kcal mol^{-1} in **P-Pyr$_4$@(Rucage)$_4$_III** (Table S1†) for the **Rucage** involved in the folding process (**Rucage-3**).

In a similar way, **P-Pyr$_4$@(Rucage)$_4$_IV** exhibits two self-folding branches, resulting in a slight increase in stability by 7.4 kcal mol^{-1} (Table 3), and similar minimum $d_{\text{Porph–Rucage}}$ distances of *ca.* 5.0 Å for the first folded **Rucage** and *ca.* 5.5 Å for the second one (Table S5†). Once again, both cages involved in the interaction with **P-Pyr$_4$** exhibit higher $|IE|$ values (Table S1†).

In **P-Pyr$_4$@(Rucage)$_4$_V** and **P-Pyr$_4$@(Rucage)$_4$_VI**, a folding of the third and fourth branches is observed, resulting in an increase in *De* of 17.3 and 69.6 kcal mol^{-1}, respectively, compared to **P-Pyr$_4$@(Rucage)$_4$_IV** (Table 3). However, in these systems, the third and fourth **Rucage** units are unable to fully interact with the porphyrin core, as evidenced by the $|IE|$ values in Table S1† and by the $d_{\text{Porph–Rucage}}$ distances of 13.1 Å (third branch, Table S5†) in **P-Pyr$_4$@(Rucage)$_4$_V** and 12.7 and 16.2 Å (third and fourth branches, Table S5†) in **P-Pyr$_4$@(Rucage)$_4$_VI** due to the steric hindrance of the other two **Rucage** units.

Overall, the scan calculations highlight that **Pyr** encapsulation is a diffusive process, given the absence of energy barriers, through the formation of non-covalent interactions detected by the IGM method. The analysis of the stability of the six **P-Pyr$_4$@(Rucage)$_4$** conformers has revealed that the folding of the branches results in an increased stability, identifying the **P-Pyr$_4$@(Rucage)$_4$_VI** model as the most stable. However, other conformers with fewer folded branches can coexist, albeit in lower proportions.

Energy transfer

Pyr → Porph. As previously mentioned, upon excitation of the pyrene chromophore in the **P-Pyr$_4$** dyad, a quenching of the **^{1}Pyr** luminescence occurs (with a decay time τ_0 = 26.3 ns and a quenched lifetime τ_q = 0.37 ns, as detailed in Table 2). This reduction is accompanied by a near-complete sensitization of the **^{1}Porph** emission. By utilizing eqn (5) and (7), we determine a fast **Pyr** to **Porph** energy transfer rate, $k_{EnT} = 2.66 \times 10^9$ s^{-1}, indicating a highly efficient energy transfer process, η_{EnT} = 0.986 (Table 4). Concerning the Förster-type mechanism governing the **Pyr** to **Porph** energy transfer process, the spectral overlap between the luminescence profile of the **Pyr** and

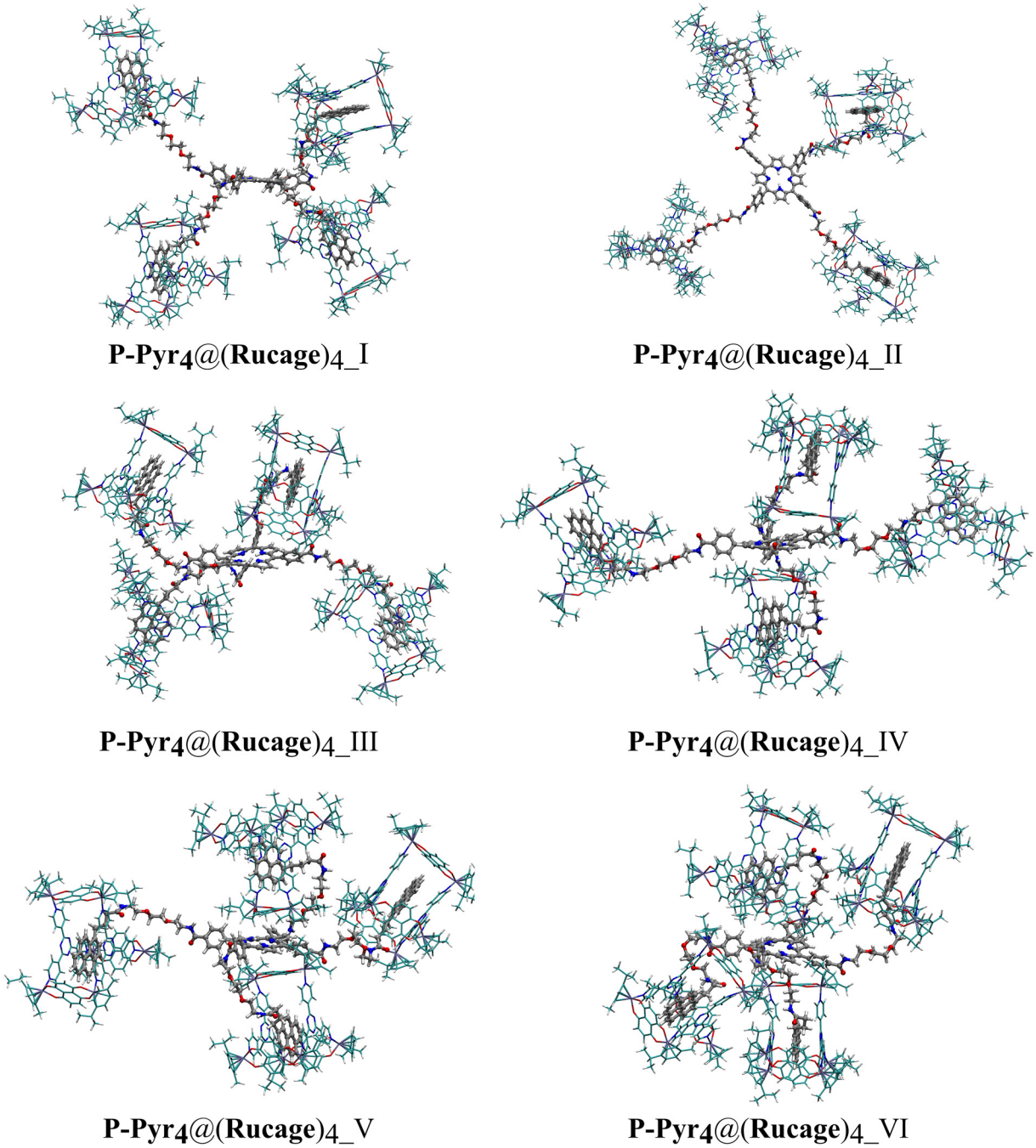

Fig. 8 Optimized structures of **P-Pyr$_4$@(Rucage)$_4$** conformations. To facilitate the visualization of the units, triflate anions are removed and the C atoms of **P-Pyr$_4$** are coloured in silver, while those of **Rucage** are reported in cyan.

Table 3 Dissociation energy (*De*), absolute values of the interaction energy (|*IE*|) and deformation energy (*Def*) in kcal mol^{-1}

Conformer	*De*	|*IE*|	*Def*
P-Pyr$_4$@(Rucage)$_4$_I	175.8	190.3	14.4
P-Pyr$_4$@(Rucage)$_4$_II	193.2	210.3	17.1
P-Pyr$_4$@(Rucage)$_4$_III	216.4	243.8	27.4
P-Pyr$_4$@(Rucage)$_4$_IV	223.8	252.5	28.7
P-Pyr$_4$@(Rucage)$_4$_V	241.1	273.7	32.6
P-Pyr$_4$@(Rucage)$_4$_VI	293.4	344.6	51.2

the absorption profile of the **TPP** models results in an overlap integral J_F = 2.18 × 10^{-13} cm^3 M^{-1} (Fig. S29† and Table 4). Utilizing κ_2 = 2/3, which accounts for a statistical distribution of the orientation factor, we calculate the corresponding critical radius R_0 = 35.7 Å (Fig. S30† and Table 4). Based on the derived J_F value, a distribution of energy transfer rate constants k_F can be obtained as a function of the interchromophoric distance d (eqn (9)). In the instance of $k_F = k_{EnT}$, the distance r = 17.6 Å accounts for the observed experimental rate

Table 4 Main parameters of the energy transfer processes

	k_{EnT}[a] (s^{-1})	η_{EnT}[b]	J_F ($cm^3\ M^{-1}$)[c]	κ^2	R_0[d] (Å)	r[e] (Å)	d[f] (Å)
Pyr → Porph	2.66×10^9	0.986	2.18×10^{-13}	0.667	35.7	17.6	20.4
Pyr → Rucage	7.51×10^7	0.027	0.68×10^{-13}	6×10^{-6}	4.2	7.7	7.7
Porph → Rucage	2.39×10^9	0.956	1.57×10^{-13}	0.667	29.9	17.9	20.3

[a] Experimental energy transfer rate constant calculated from eqn (5) and (6). [b] Experimental efficiency of the energy transfer process calculated from eqn (7). [c] Overlap integral calculated from eqn (10). [d] Förster critical distance calculated from eqn (8). [e] Interchromophoric distance calculated for $k_F = k_{EnT}$. [f] Average donor–to–acceptor interchomophoric distance calculated from molecular modelling.

constant value (Fig. S30†). This distance is comparable to the average **Pyr** donor to **Porph** acceptor separation (d = 20.4 Å, Fig. S31†) inferred from the molecular modelling of the **P-Pyr$_4$** dyad (Fig. 8 and S25†).

Pyr → Rucage. In the **P-Pyr$_4$@(Rucage)$_4$** system, the lifetime of the **Pyr** moiety (τ_0 = 0.37 ns in the **P-Pyr$_4$** model) remains nearly unchanged despite the presence of the **Rucage**, τ_q = 0.36 ns. This indicates a highly inefficient (η_{EnT} = 0.027) and slow ($k_{EnT} = 7.5 \times 10^7\ s^{-1}$) energy transfer process. Thus, despite the close proximity of the pyrene donor to the naphtoquinonato acceptor, virtually no energy transfer is observed. Utilizing the Förster model and the available spectroscopic data, the overlap integral $J_F = 0.68 \times 10^{-13}\ cm^3\ M^{-1}$ can be computed (Fig. S32 and S33†), which is only three times smaller than the corresponding value calculated for the **Pyr** to **Porph** energy transfer process (Table 4). It is important to note that the pyrenyl moiety in the **P-Pyr$_4$@(Rucage)$_4$** system is confined within the **Rucage**, oriented between the two trispyridyltriazine panels in a parallel fashion. In this arrangement, the pyrene consistently maintains an orthogonal orientation to the naphtoquinonato pillars (Fig. 8 and S26†). Since the transition dipoles align parallel to the aromatic rings of both the pyrene donor and the naphtoquinonato acceptor, they consequently form an angle close to 90°, resulting in $\kappa_2 \sim 0$. The molecular modelling provides an average donor–to–acceptor interchromophoric distance of d = 7.7 Å (Fig. S34†), yielding $\kappa_2 = 6 \times 10^{-6}$ for $k_F = k_{EnT}$.

Porph → Rucage. Upon excitation of the porphyrin donor in the **P-Pyr$_4$@(Rucage)$_4$** system, a complex behaviour of the luminescence decay of the **^{1}Porph** excited state is observed, as discussed above. In particular, beside the ultrafast (τ < 300 fs) and long-lived (τ = 9.1 ns) components, a lifetime τ_q = 400 ps has been observed (Table 2), attributable to quenching by an energy transfer process. This leads to a rate and efficiency of the **Porph** to **Rucage** energy transfer process of $k_{EnT} = 2.39 \times 10^9$ and η_{EnT} = 0.956, respectively (Table 4). By applying the Förster analysis to the **TPP–Rucage** model system, an overlap integral $J_F = 1.57 \times 10^{-13}\ cm^3\ M^{-1}$ (Fig. S35†) comparable to that obtained for the **Pyr–TPP** couple, but whit a slightly shorter critical radius (R_0 = 29.9 Å), is calculated (Fig. S36† and Table 4). Based on these parameters, an interchromophoric distance $r \sim 18$ Å, to be compared with the average value calculated for the DFT-based models ($d \sim 20$ Å, Fig. S37 and S38†), accounts for the observed energy transfer efficiency (Table 4).

Conclusions

A novel supramolecular system has been assembled by combining a tetrapyrenylporphyrinic core with arene–ruthenium metalla-prisms, the latter being able to encapsulate the pyrenyl residues, thus leading to a large complex which is stable and does not aggregate in DCM solution. Detailed electrochemical and photophysical investigations elucidated the complex excited state dynamics of the supramolecular array. Femtosecond transient absorption analysis, in particular, evidenced fast excited states deactivation processes in the arene–ruthenium complexes, which were found to be non-emissive both at room temperature and at 77 K, and energy and electron transfer processes in the complete array. Different kinetics have been observed for the photoinduced reactions occurring between the central porphyrin core and the peripheral metalla-cages, indicating the presence in solution of various conformations, where the components are placed at different distances. Detailed computational analysis elucidated the stability of the different conformations and the encapsulation interactions between the pyrenyl groups and the metalla-cages. The results show novel photophysical insights on pyrenyl-functionalized porphyrins/metalla arene–ruthenium structures, that can lead to promising applications in biological and energy conversion contexts.

Author contributions

Conceptualization, verification and funding acquisition: B. T., B. V.; investigation: S. L. P. A., B. V., A. B.; formal analysis: D. V.; data curation, writing – original draft and writing – review and editing: all authors.

Data availability

Data supporting this article have been presented in the ESI.†

Conflicts of interest

There are no conflicts to declare.

Note after first publication

This article replaces the version published on 20th January 2025, which contained an incorrect version of eqn (2) due to a production error.

Acknowledgements

We thank the European Union for financial support for the H2020-MSCA-ITN-2017-765297 project "NOAH". Italian CNR (Project "Light-Induced Processes (LIP)") is also acknowledged.

References

1 M. D. Karkas, O. Verho, E. V. Johnston and B. Akermark, *Chem. Rev.*, 2014, **114**, 11863–12001.
2 O. M. Ogba, N. C. Warner, D. J. O'Leary and R. H. Grubbs, *Chem. Soc. Rev.*, 2018, **47**, 4510–4544.
3 A. Carella, F. Borbone and R. Centore, *Front. Chem.*, 2018, **6**, 481.
4 C. E. Elgar, N. A. Yusoh, P. R. Tiley, N. Kolozsvari, L. G. Bennett, A. Gamble, E. V. Pean, M. L. Davies, C. J. Staples, H. Ahmad and M. R. Gill, *J. Am. Chem. Soc.*, 2023, **145**, 1236–1246.
5 M. R. Gill and J. A. Thomas, *Chem. Soc. Rev.*, 2012, **41**, 3179–3192.
6 N. P. Barry, O. Zava, J. Furrer, P. J. Dyson and B. Therrien, *Dalton Trans.*, 2010, **39**, 5272–5277.
7 J. Mattsson, O. Zava, A. K. Renfrew, Y. Sei, K. Yamaguchi, P. J. Dyson and B. Therrien, *Dalton Trans.*, 2010, **39**, 8248–8255.
8 F. E. Poynton, S. A. Bright, S. Blasco, D. C. Williams, J. M. Kelly and T. Gunnlaugsson, *Chem. Soc. Rev.*, 2017, **46**, 7706–7756.
9 J. W. Yi, N. P. Barry, M. A. Furrer, O. Zava, P. J. Dyson, B. Therrien and B. H. Kim, *Bioconjugate Chem.*, 2012, **23**, 461–471.
10 J. Shirdel, A. Penzkofer, R. Procházka, Z. Shen, J. Strauss and J. Daub, *Chem. Phys.*, 2007, **331**, 427–437.
11 B. Therrien, *CrystEngComm*, 2015, **17**, 484–491.
12 E. Orhan, A. Garci and B. Therrien, *Inorg. Chim. Acta*, 2017, **461**, 78–83.
13 F. Schmitt, N. P. Barry, L. Juillerat-Jeanneret and B. Therrien, *Bioorg. Med. Chem. Lett.*, 2012, **22**, 178–180.
14 V. Vajpayee, Y. J. Yang, S. C. Kang, H. Kim, I. S. Kim, M. Wang, P. J. Stang and K.-W. Chi, *Chem. Commun.*, 2011, **47**, 5184–5186.
15 N. P. E. Barry and B. Therrien, *Eur. J. Inorg. Chem.*, 2009, **2009**, 4695–4700.
16 J. Freudenreich, N. P. E. Barry, G. Süss-Fink and B. Therrien, *Eur. J. Inorg. Chem.*, 2010, **2010**, 2400–2405.
17 J. Mattsson, P. Govindaswamy, J. Furrer, Y. Sei, K. Yamaguchi, G. Süss-Fink and B. Therrien, *Organometallics*, 2008, **27**, 4346–4356.
18 D. Chen, T. Xiao, E. Monflier and L. Wang, *Commun. Chem.*, 2024, **7**, 88.
19 K. Acharyya, S. Bhattacharyya, H. Sepehrpour, S. Chakraborty, S. Lu, B. Shi, X. Li, P. S. Mukherjee and P. J. Stang, *J. Am. Chem. Soc.*, 2019, **141**, 14565–14569.
20 D. Li, X. Liu, L. Yang, H. Li, G. Guo, X. Li and C. He, *Chem. Sci.*, 2023, **14**, 2237–2244.
21 Y. Li, S. S. Rajasree, G. Y. Lee, J. Yu, J. H. Tang, R. Ni, G. Li, K. N. Houk, P. Deria and P. J. Stang, *J. Am. Chem. Soc.*, 2021, **143**, 2908–2919.
22 A. Sautter, B. K. Kaletas, D. G. Schmid, R. Dobrawa, M. Zimine, G. Jung, I. H. van Stokkum, L. De Cola, R. M. Williams and F. Wurthner, *J. Am. Chem. Soc.*, 2005, **127**, 6719–6729.
23 Z. Zhang, Z. Zhao, Y. Hou, H. Wang, X. Li, G. He and M. Zhang, *Angew. Chem., Int. Ed.*, 2019, **58**, 8862–8866.
24 P. P. Jia, L. Xu, Y. X. Hu, W. J. Li, X. Q. Wang, Q. H. Ling, X. Shi, G. Q. Yin, X. Li, H. Sun, Y. Jiang and H. B. Yang, *J. Am. Chem. Soc.*, 2021, **143**, 399–408.
25 T. T. Kim Cuc, P. Q. Nhien, T. M. Khang, H.-Y. Chen, C.-H. Wu, B.-T. B. Hue, Y.-K. Li, J. I. Wu and H.-C. Lin, *ACS Appl. Mater. Interfaces*, 2021, **13**, 20662–20680.
26 J. Otsuki, *J. Mater. Chem. A*, 2018, **6**, 6710–6753.
27 G. Chen, F. Song, X. Xiong and X. Peng, *Ind. Eng. Chem. Res.*, 2013, **52**, 11228–11245.
28 L. Yuan, W. Lin, K. Zheng and S. Zhu, *Acc. Chem. Res.*, 2013, **46**, 1462–1473.
29 T. Chen, B. He, J. Tao, Y. He, H. Deng, X. Wang and Y. Zheng, *Adv. Drug Delivery Rev.*, 2019, **143**, 177–205.
30 M. Dimura, T. O. Peulen, C. A. Hanke, A. Prakash, H. Gohlke and C. A. Seidel, *Curr. Opin. Struct. Biol.*, 2016, **40**, 163–185.
31 F. C. Ho, Y. J. Huang, C. C. Weng, C. H. Wu, Y. K. Li, J. I. Wu and H. C. Lin, *ACS Appl. Mater. Interfaces*, 2020, **12**, 53257–53273.
32 H. L. Anderson, S. Anderson and J. K. M. Sanders, *J. Chem. Soc., Perkin Trans. 1*, 1995, 2231–2245.
33 N. P. Barry, F. Edafe and B. Therrien, *Dalton Trans.*, 2011, **40**, 7172–7180.
34 T. Gianferrara, A. Bergamo, I. Bratsos, B. Milani, C. Spagnul, G. Sava and E. Alessio, *J. Med. Chem.*, 2010, **53**, 4678–4690.
35 G. A. Crosby and J. N. Demas, *J. Phys. Chem.*, 1971, **75**, 991–1024.
36 I. B. Berlman, in *Handbook of Fluorescence Spectra of Aromatic Molecules*, ed. A. Press, New York and London, 2nd edn, 1971, p. 296.
37 P. G. Seybold and M. Gouterman, *J. Mol. Spectrosc.*, 1969, **31**, 1–13.
38 K. A. Nguyen, P. N. Day and R. Pachter, *J. Chem. Phys.*, 2011, **135**, 074109.
39 A. Schafer, H. Horn and R. Ahlrichs, *J. Chem. Phys.*, 1992, **97**, 2571–2577.
40 A. Schafer, C. Huber and R. Ahlrichs, *J. Chem. Phys.*, 1994, **100**, 5829–5835.
41 A. V. Marenich, C. J. Cramer and D. G. Truhlar, *J. Phys. Chem. B*, 2009, **113**, 6378–6396.

42 C. Adamo and D. Jacquemin, *Chem. Soc. Rev.*, 2013, **42**, 845–856.
43 A. D. Laurent, C. Adamo and D. Jacquemin, *Phys. Chem. Chem. Phys.*, 2014, **16**, 14334–14356.
44 F. Neese, *Wiley Interdiscip. Rev.:Comput. Mol. Sci.*, 2022, **12**, e1606.
45 C. Bannwarth, S. Ehlert and S. Grimme, *J. Chem. Theory Comput.*, 2019, **15**, 1652–1671.
46 S. Grimme, C. Bannwarth and P. Shushkov, *J. Chem. Theory Comput.*, 2017, **13**, 1989–2009.
47 P. Pracht, E. Caldeweyher, S. Ehlert and S. Grimme, *ChemRxiv*, 2019, preprint, DOI: 10.26434/chemrxiv.8326202.v1.
48 C. Bannwarth, E. Caldeweyher, S. Ehlert, A. Hansen, P. Pracht, J. Seibert, S. Spicher and S. Grimme, *Wiley Interdiscip. Rev.: Comput. Mol. Sci.*, 2021, **11**, e01493.
49 S. Ehlert, M. Stahn, S. Spicher and S. Grimme, *J. Chem. Theory Comput.*, 2021, **17**, 4250–4261.
50 S. Halbert and H. Gérard, *New J. Chem.*, 2015, **39**, 5410–5419.
51 E. Pancani, D. Veclani, M. Agnes, A. Mazza, A. Venturini, M. Malanga and I. Manet, *RSC Adv.*, 2023, **13**, 10923–10939.
52 *Principles of Fluorescence Spectroscopy*, ed. J. R. Lakowicz, Springer US, Boston, MA, 2006, pp. 443–475.
53 M. A. Furrer, F. Schmitt, M. Wiederkehr, L. Juillerat-Jeanneret and B. Therrien, *Dalton Trans.*, 2012, **41**, 7201–7211.
54 A completely irreversible oxidation process, located at ca. E_{peak} = +0.80 V, probably attributable to the generation of a reduced species during the cathodic scan, is also observed.
55 A lifetime of 400 ps has been fixed in the analysis, in order to match the 400 ps component measured with single photon counting analysis of the luminescence decay.
56 E. A. Alemán, J. Manríquez Rocha, W. Wongwitwichote, L. A. Godínez Mora-Tovar and D. A. Modarelli, *J. Phys. Chem. A*, 2011, **115**, 6456–6471.
57 J. Fajer, D. C. Borg, A. Forman, D. Dolphin and R. H. Felton, *J. Am. Chem. Soc.*, 1970, **92**, 3451–3459.
58 S. Durot, L. Flamigni, J. Taesch, T. T. Dang, V. Heitz and B. Ventura, *Chem. – Eur. J.*, 2014, **20**, 9979–9990.
59 T. T. Dang, S. Durot, L. Monnereau, V. Heitz, A. Barbieri and B. Ventura, *Dalton Trans.*, 2017, **46**, 9375–9381.
60 Single wavelength decay analysis of the transient matrix of **P-Pyr$_4$@(Rucage)$_4$** leads to identify a component of *ca.* 400 ps, which can be different in the global analysis due to the complex overlay of signals.
61 M. Gouterman and G.-E. Khalil, *J. Mol. Spectrosc.*, 1974, **53**, 88–100.
62 J. A. S. Cavaleiro, H. Görner, P. S. S. Lacerda, J. G. MacDonald, G. Mark, M. G. P. M. S. Neves, R. S. Nohr, H.-P. Schuchmann, C. von Sonntag and A. C. Tomé, *J. Photochem. Photobiol. A: Chem.*, 2001, **144**, 131–140.
63 The same result has been obtained upon excitation of **Clip-2**, **Rucage** and **P-Pyr$_4$@(Rucage)$_4$** at 700 nm.
64 C. Lefebvre, H. Khartabil, J. C. Boisson, J. Contreras-Garcia, J. P. Piquemal and E. Henon, *ChemPhysChem*, 2018, **19**, 724–735.
65 C. Lefebvre, G. Rubez, H. Khartabil, J. C. Boisson, J. Contreras-Garcia and E. Henon, *Phys. Chem. Chem. Phys.*, 2017, **19**, 17928–17936.